

Article

## A Synergistic Methodology for Soil Moisture Estimation in an Alpine Prairie Using Radar and Optical Satellite Data

Binbin He \*, Minfeng Xing and Xiaojing Bai

School of Resources and Environment, University of Electronic Science and Technology of China, No. 2006, Xiyuan Ave, West Hi-Tech Zone, Chengdu 611731, China;

E-Mails: xingminfeng@163.com (M.X.); baixiaojing1219@126.com (X.B.)

\* Author to whom correspondence should be addressed; E-Mail: binbinhe@uestc.edu.cn; Tel.: +86-28-6183-1571.

External Editors: George P. Petropoulos and Prasad S. Thenkabail

Received: 22 June 2014; in revised form: 18 September 2014 / Accepted: 29 September 2014 /

Published: 10 November 2014

---

**Abstract:** This paper presents a microwave/optical synergistic methodology to retrieve soil moisture in an alpine prairie. The methodology adequately represents the scattering behavior of the vegetation-covered area by defining the scattering of the vegetation and the soil below. The Integral Equation Method (IEM) was employed to determine the backscattering of the underlying soil. The modified Water Cloud Model (WCM) was used to reduce the effect of vegetation. Vegetation coverage, which can be easily derived from optical data, was incorporated in this method to account for the vegetation gap information. Then, an inversion scheme of soil moisture was developed that made use of the dual polarizations (HH and VV) available from the quad polarization Radarsat-2 data. The method developed in this study was assessed by comparing the reproduction of the backscattering, which was calculated from an area with full vegetation cover to that with relatively sparse cover. The accuracy and sources of error in this soil moisture retrieval method were evaluated. The results showed a good correlation between the measured and estimated soil moisture ( $R^2 = 0.71$ , RMSE = 3.32 vol.%,  $p < 0.01$ ). Therefore, this method has operational potential for estimating soil moisture under the vegetated area of an alpine prairie.

**Keywords:** soil moisture; remote sensing; microwave/optical synergistic methodology; vegetated area; Integral Equation Method (IEM); Water Cloud Model (WCM)

---

## 1. Introduction

Information about distributed surface soil moisture content is important for assessing water availability for plant growth in alpine prairies because it impacts the length of the grazing season, the grass growth rate and nutrient uptake. Unfortunately, the spatial and temporal variations of soil moisture cannot be easily observed at large scales using conventional measurement techniques. Satellite remote sensing provides a uniquely effective and efficient means of monitoring and assessing soil moisture.

The change in the soil dielectric constant as a result of variation in soil moisture content has more influence than other characteristics [1]. Therefore, radar remote sensing is sensitive to soil moisture because its dielectric constant is one of the most important factors in radar backscattering intensity [2]. A number of models that simulate soil moisture based on synthetic aperture radar (SAR) data have been developed for bare soil [3–9]. However, these models cannot be applied directly in vegetated areas due to the scattering of vegetation [10]. Vegetation canopies complicate the retrieval of moisture in the underlying soil because canopies contain moisture of their own [11]. Thus, SAR acquisition corresponds to the combined signatures of vegetation and soil water [12,13]. Due to multiple scattering effects of the canopies, the interaction between the contributions of soil moisture, vegetation and observed backscattering is highly nonlinear [11,14]. Therefore, the key problem in the quantitative estimation of soil moisture is to separate the contributions of vegetation backscatter and vegetation-covered soil moisture backscattering from the observed backscattering.

To use SAR data for soil moisture estimation in a vegetated area, vegetation effects have been considered in several studies using vegetation scattering models [11,15–18]. The effects of vegetation on the SAR signature are controlled by its biophysical parameters (e.g., vegetation coverage and leaf area index), which can be derived by optical remote sensing. The vegetation parameters can be used to quantify vegetation attenuation of radar signals in radiative transfer function models [19]. To minimize the effect of vegetation, some researchers [14,20–22] have attempted to use additional vegetation information provided by optical remote sensing, which has been widely used to derive information of vegetation properties. Furthermore, other studies [14,23] have suggested that the accuracy of soil moisture estimates was significantly improved when optical and SAR data were combined as compared to estimates from SAR data only.

Despite many successful retrieval studies and promising results achieved, some issues in mountain areas still remain unexplored and further research is required [24,25]. The retrieval from remote sensing is much more challenging because of the presence of topography. In this paper, a synergistic method for applying optical and SAR remote sensing data to estimate soil moisture in a vegetated area was developed. The method was based on the vegetation coverage for calculating the contribution of the fraction of vegetation and bare soil at the pixel level to better represent the difference in the scattering mechanisms between vegetation and bare soil. The vegetation information was extracted from optical remote sensing to correct the SAR observations for the vegetation effects based on the Water Cloud Model (WCM) [26]. Thirty meter resolution digital elevation model (DEM) data were used to correct terrain-induced distortions in the SAR data. The vegetation correction procedure was embedded within a soil moisture retrieval algorithm for which the surface scattering component was formulated by the Integral Equation Method (IEM) [6]. Then, the developed method was applied to estimate soil moisture in the alpine grassland.

## 2. Study Area and Data

### 2.1. Study Area and Ground Data

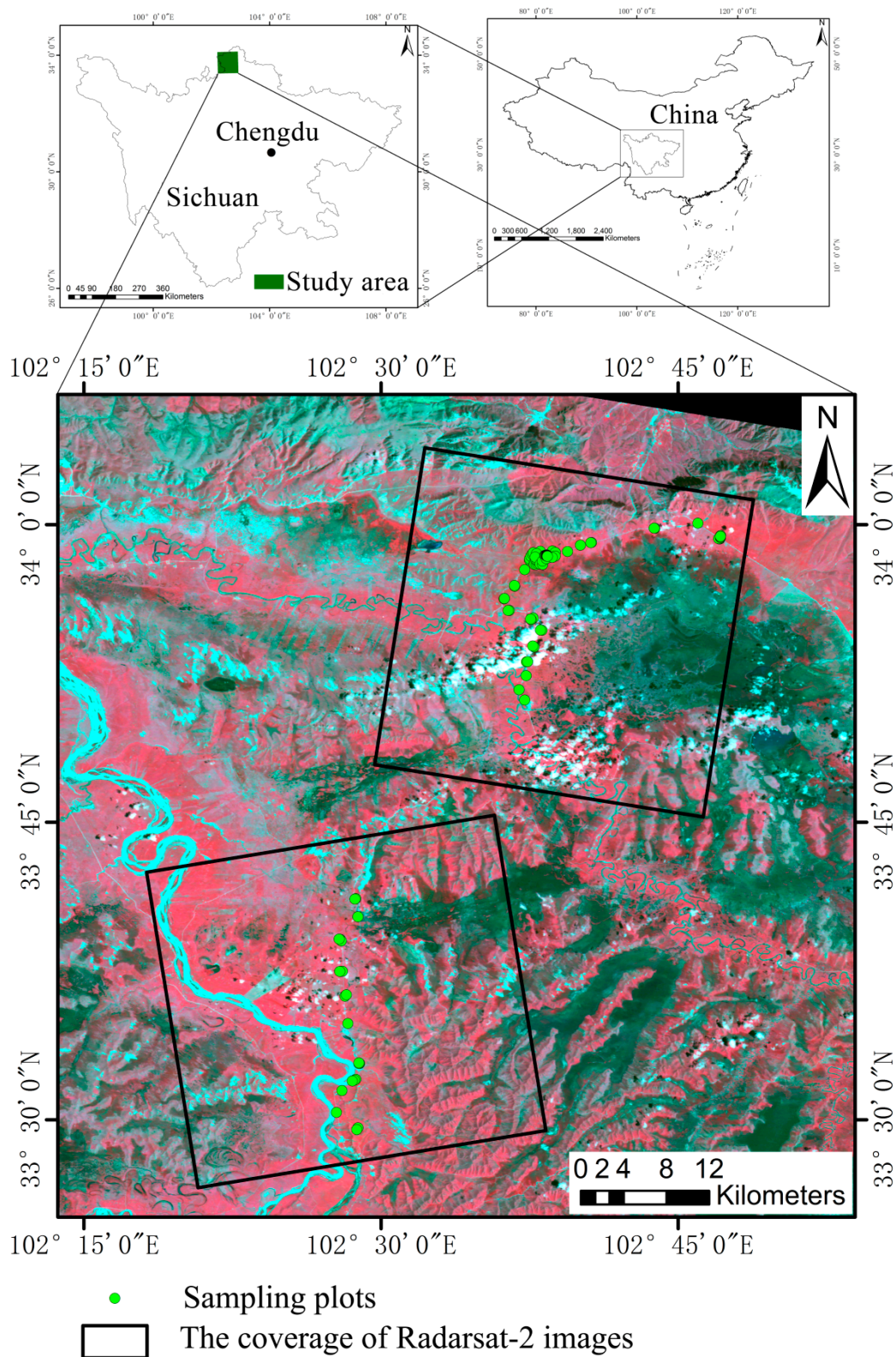
The field campaign was conducted over an alpine grassland located in the eastern part of the Qinghai-Tibet Plateau of China, called Ruoergai Prairie (approximately centered at 33°37'N; 102°54'E) (Figure 1). Ruoergai Prairie has a cold, humid plateau monsoonal climate with an average annual temperature of 0.7 °C and a total precipitation of 656.8 mm [27]. It is characterized by rolling hills that range from 3422 m to 3704 m in elevation. The frozen period of the Ruoergai Prairie is eight months. The snow begins to fall in October.

Coincident with the Radarsat-2 satellite overpasses, field campaign measurements of soil moisture and vegetation parameters were conducted over the study area. There are 97 sampling sites along a road distributed over the study area. Topography of the sampling sites is relatively flat. Each sampling site was 30 m × 30 m. Within each sampling site, soil moisture was measured using a Time-Domain Reflectometer (TDR) probe (Model CS659, manufactured by Campbell Scientific) at a soil layer of approximately 10 cm by inserting the rod into the ground vertically and characterized by a relative accuracy of 3% (Campbell Scientific, <http://www.campbellsci.com/cs659>). To reduce the measurement error, soil moisture was measured ten times at each of the sampling sites, and the average was then computed. Soil samples for moisture measurements in 50 sampling sites were also taken to calibrate the TDR. However, due to the small number of soil samples, it is possible that the calibration of TDR was imperfect. Meanwhile, the following parameters were measured in 50 sampling sites: vegetation biomass, leaf area index (LAI), vegetation height, vegetation water content, vegetation coverage, single leaf area, leaf density, physiological and biochemical parameters, leaf structure parameters and vegetation spectral properties. The vegetation biomass samples were clipped from three randomly selected plots (0.5 m × 0.5 m) within each sampling site weighed *in situ*, and dried in an oven at 120 °C for 30 min and then at 80 °C for 24 h. An LAI-2200 instrument was used to measure the LAI. The LAI was evenly measured for ten times. The average value of ten LAI values was considered to represent the LAI value of the sampling site. The average value of the measured biomass in the three plots was assumed to represent the value of the full sample site. The water content of samples was determined by weighing each sample before and after oven drying to estimate the vegetation water content (wet weight minus dry weight). A Full Range Portable Spectroradiometer (PSR-3500) was used for vegetation spectral measurements. In addition, to avoid mixed-pixel problem, the sampling sites were restricted to a distance of at least 300 m away from the roads.

### 2.2. Optical Remote Sensing Data

The Environment and Disaster Monitoring and Forecasting by Small Satellite Constellation A and B satellites (HJ-1 A/B satellites) were launched by China in 2008. The charge-coupled device (CCD) camera is one of the instruments that operate on the HJ-1A and HJ-1B satellites. Each satellite provides a spatial resolution of 30 m, a swath width of 700 km, and a four day return period. The combination of the two satellites is capable of providing a two day return period. The HJ-1 CCD cameras have three visible bands (0.43–0.52 μm, 0.52–0.60 μm, and 0.63–0.69 μm) and one near-infrared (NIR) band (0.76–0.9 μm).

**Figure 1.** Location of study region and the distribution of sampling plots in the study area. The background image is a charge-coupled device (CCD) composite image of bands 4 (near-infrared), 3 (red), and 2 (green) (corresponding to R, G, B color space) showing the study area.



The HJ-1A CCD1 image was collected during virtually cloud-free conditions on 4 August 2013. The following steps were used to preprocess the HJ-1 CCD image.

(1) Geometric correction: The images were geometrically referenced using a set of 30 ground control points measured by a differential global positioning system (GPS) unit. The root mean square error (RMSE) of the geometric correction was less than one pixel, which meets the geometry correction requirement.

(2) Radiometric calibration: First, the DN values of the raw image were converted to the at-satellite radiance using calibration coefficients (Table 1) provided by the China Center for Resources Satellite Data and Application. The calibration equation used is

$$L = DN / \alpha + L_o \quad (1)$$

where  $L$  is the apparent radiance,  $DN$  is the digital number of the raw image,  $\alpha$  is the absolute calibration coefficient, and  $L_o$  is the offset.

The apparent radiance was then converted to apparent reflectance according to

$$\rho_\lambda = \frac{\pi \times L_\lambda \times D^2}{E_{sun\lambda} \times \cos \theta} \quad (2)$$

where  $\rho_\lambda$  is the apparent reflectance of the band  $\lambda$  at the top of the atmosphere,  $D$  is the distance of the astronomical unit from the earth to the sun,  $\theta$  is the solar zenith angle, and  $E_{sun}$  is the mean exoatmospheric solar irradiance in the  $\lambda$ . The exoatmospheric solar irradiance for HJ-1A CCD1 is listed in Table 1.

(3) Atmospheric correction: the algorithm of 6S (the second simulation of the satellite signal in the solar spectrum) [28], an atmospheric radiative transfer model, and HJ-1 CCD spectral response function were used to convert sensor radiance to directional surface reflectance. The study area is at the mid-latitude in summer and the aerosol type is continental. The parameters were inputted into the 6S code with surface assumption of non-uniform Lambertian to correct HJ-1 CCD image, and the outcome was atmospherically corrected reflective radiation.

**Table 1.** Absolute radiometric calibration coefficient and exoatmospheric solar irradiance for HJ-1A CCD1.

HJ-1A CCD1	$\alpha$	$L_o$	$E_{sun\lambda}$
<b>Band 1</b>	0.7696	7.3250	1914.324
<b>Band 2</b>	0.7815	6.0737	1825.419
<b>Band 3</b>	1.0914	3.6123	1542.664
<b>Band 4</b>	1.0281	1.9028	1073.826

### 2.3. Radarsat-2 Data

Radarsat-2 has a C-band (approximately 5.6 cm wavelength) quad-polarized SAR sensor onboard with multiple configuration and polarization modes. Two SAR images were acquired on 4 August (descending orbit 29,446, center incidence angle of 37.2°) and 7 August 2013 (ascending orbit 29,482, center incidence angle of 31.1°), over the study area. The acquisition mode was fine quad polarization, right looking, and with a nominal spatial resolution of 8 m. The impact of different orbits is construed

as minimal due to the relatively flat terrain in the sampling sites. Radiometric calibrations of the Radarsat-2 images were performed using calibration tools included in the Next ESA SAR toolbox (NEST), which were provided by the European Space Agency. The images were then projected using the Universal Transverse Mercator (UTM) (Zone 48N, World Geodetic System (WGS) 84). These products were then geometrically corrected using a set of 40 control points taken from the HJ-1 CCD image, which had been accurately corrected. The control points were evenly distributed, and the RMSE was less than 1.5 pixels for both Radarsat-2 SAR images. For speckle reduction, the SAR images were filtered using the  $5 \times 5$  refined Lee speckle filter [29]. Finally, the pixel sizes of the Radarsat-2 fine quad images were resampled to a  $30 \text{ m} \times 30 \text{ m}$  resolution to facilitate integration with the HJ-1 CCD data.

Topography has a significant influence on the radiometric properties of SAR images [30]. In this study, 30 m resolution DEM data were used to correct terrain-induced distortions in the Radarsat-2 data. Based on the method introduced by van Zyl [31], the backscattering coefficient of the SAR image was corrected to a reference surface:

$$\sigma_{cor}^o = \sigma^o \times \frac{\sin \eta \cos \theta_\alpha}{\sin \eta_0} \quad (3)$$

where  $\sigma_{cor}^o$  is the topographically corrected backscattering of each pixel.  $\eta$  is the local incidence angle,  $\theta_\alpha$  is the azimuth slope, and  $\eta_0$  is the SAR incidence angle recorded in the metadata.

$\eta$  was calculated as follows [32]:

$$\cos \eta = \cos \theta \cos \eta_0 + \sin \theta \sin \eta_0 \cos \Delta\varphi \quad (4)$$

where  $\theta$  is the local slope angle and  $\Delta\varphi$  is the relative azimuth angle between the local aspect and SAR azimuth.

The azimuth slope  $\theta_\alpha$  can be determined from the following relationship [19]:

$$\tan \theta_\alpha = \tan \theta \sin \Delta\varphi \quad (5)$$

Radar shadows and layovers occur in areas with high relief and steep slopes when  $\theta > \eta_0$  or  $\eta > 90^\circ$  [19]. The topographic effects were irreversible in areas with layovers and shadows. These areas (less than 3.5% in this study area) were masked out in the process.

### 3. Methods

Radar backscattering responds to surface roughness and soil moisture; however, in a vegetated area, it can also be affected by vegetation cover and plant water content [18,33–35]. Therefore, the backscattering from the vegetated area consists of the volume scattering from the vegetation and the surface scattering from the underlying soil. In addition, the signal scattering from the underlying soil is attenuated by the vegetation layer.

In this study, a microwave/optical synergistic model to simulate the radar backscattering from a vegetated surface based on the WCM [26] and IEM [6] was developed. The IEM was used to simulate the scattering from a bare soil surface, and the WCM was used to calculate the volume scattering and the two-way attenuation from the vegetation. In addition, the synergistic model included usage of the vegetation cover fractions derived from optical remote sensing data for the vegetation gap information. Then, the soil moisture was estimated by applying the inverted model.

### 3.1. Bare Soil Scattering

The backscattering from a bare soil surface mainly depends on the soil moisture content and soil surface roughness [17]. To determine the backscattering of the underlying soil ( $\sigma_{soil}^o$ ), the IEM [6] was employed in this study. In general, the IEM quantifies the backscattering coefficient from a surface as a function of its roughness parameters, its dielectric constant, and the characteristics of the acquired images (polarization, incidence angle, and frequency). The soil roughness is characterized by the root mean square height and correlation length. The dielectric constant is derived from the surface volumetric moisture content [33]. In this study, the dielectric constant was calculated by the Topp model [36], which was validated for a wide range of soils under different conditions [37]. In a prairie environment, the vegetation complicates the assessment of the soil roughness. To overcome this problem, the surface height and the autocorrelation length was estimated using the method proposed by Magagi *et al.* [38] over the bare area.

### 3.2. Effect of Vegetation

#### 3.2.1. Vegetation Backscattering Model

The IEM was originally developed to describe the scattering from bare soil surfaces only; therefore, vegetation backscattering effects are not explicitly incorporated in the model [11]. In this study, the WCM [26] was used to reduce the effect of vegetation. The WCM, introduced by Attema and Ulaby [26], was developed for predicting the backscattering from a vegetated area. In this study, the basic structure of the WCM was adopted for characterizing the backscattering in our study area.

The WCM, which is a first-order approximation of the radiation transferred from vegetation canopies using empirical coefficients and parameters, assumes that vegetation consists of a collection of spherical water droplets that are structurally held in place by dry matter [11]. In the WCM, the total backscattering ( $\sigma^o$ ) is represented as the incoherent sum of the contribution of the vegetation ( $\sigma_{veg}^o$ ) and the contribution of the underlying soil ( $\sigma_{soil}^o$ ), which is attenuated by the vegetation layer. Thus, the WCM can be represented by the following equation:

$$\sigma^o = \sigma_{veg}^o + \tau^2 \sigma_{soil}^o \quad (6)$$

where

$$\sigma_{veg}^o = AV_1 \cos(1 - \tau^2) \quad (7)$$

$$\tau^2 = \exp(-2BV_2 / \cos \theta) \quad (8)$$

In these equations,  $\tau^2$  is the two-way attenuation through the canopy,  $V_1$  is a description of the canopy,  $\theta$  is an incident angle, and  $V_2$  is a second description of the canopy. Because an important part of the scattering and attenuation is controlled by the leaves, many studies [17,39,40] propose using the LAI as the canopy descriptor. In this study, the canopy descriptors  $V_1$  and  $V_2$  were associated with the LAI, *i.e.*,  $V_1 = V_2 = LAI$ . The LAI was estimated from the optical imagery using PROSAIL model [41].  $A$  and  $B$  are empirical coefficients that depend on the canopy type [40,42]. To estimate the vegetation parameter  $A$ , Michigan Microwave Canopy Scattering model (MIMICS) [43] was used to calculate vegetation backscattering coefficients  $\sigma_{veg}^o$  at locations where ground-based measurements of

soil and other ancillary data are available. Then, the value of  $A$  was derived using the least squares method. The attenuation factor ( $\tau$ ) in Equation (6) was calculated using the method described by Wang [19]. Then, the value of  $B$  was obtained using the least squares method. The IEM model was used to replace  $\sigma_{soil}^o$  in the WCM model. This replacement allows for a more realistic soil moisture contribution in the total backscattering of Equation (6) [2].

### 3.2.2. Modification of the Vegetation Backscattering Model

One assumption of the WCM described in Section 3.2.1 is that volume scattering is the predominant mechanism responsible for the backscattering from vegetation [26]. However, in the actual environment, vegetation is usually unevenly distributed and does not satisfy this assumption. Because of the strong influence from the underlying ground surface in sparse vegetation cover areas, the backscattering contribution of bare soil surfaces must be considered a key component in the total backscattering. In a previous study, the total backscattering was divided into the contributions from the surface covered by vegetation and the fraction representing direct backscattering from bare soil surfaces [44–46]. In this study, the scattering mechanism for the vegetation cover component and bare soil component in a pixel were separated by vegetation coverage. First, the backscattering was calculated using a vegetation backscattering model under the assumption that a pixel was fully covered by vegetation. Then, the actual backscattering coefficient from the fraction of the surface covered by vegetation was calculated based on the vegetation coverage. Then, the actual backscattering coefficient from the fraction of the surface covered by vegetation was calculated based on the vegetation coverage. Similarly, the actual backscattering coefficient for the fraction representing direct backscattering from the bare soil surface was calculated using the fraction of the bare soil. Therefore, the total backscattering from a pixel can be expressed as:

$$\sigma_{total}^o = f_{veg} \sigma^o + (1 - f_{veg}) \sigma_{soil}^o \quad (9)$$

where  $f_{veg}$  is the vegetation coverage.  $\sigma_{soil}^o$  can be calculated using the IEM.

Equation (9) may be combined with Equation (6) and rewritten as:

$$\sigma_{total}^o = f_{veg} (\sigma_{veg}^o + \tau^2 \sigma_{soil}^o) + (1 - f_{veg}) \sigma_{soil}^o \quad (10)$$

In this study, the vegetation coverage was delineated using a Dimidiate Pixel Model (DPM) [47] with optical remote sensing data. Thus, vegetation coverage ( $f_{veg}$ ) can be expressed as:

$$f_{veg} = \frac{NDVI - NDVI_{min}}{NDVI_{max} - NDVI_{min}} \quad (11)$$

where  $NDVI$  is the normalized difference vegetation index calculated from the HJ-1 CCD data.  $NDVI_{max}$  and  $NDVI_{min}$  are the normalized difference vegetation indexes of an area covered by full green vegetation and bare soil, respectively. In the DPM, the  $NDVI$  of a pixel is the sum of the complete vegetation  $NDVI$  ( $NDVI_{max}$ ) and the non-vegetation  $NDVI$  ( $NDVI_{min}$ ).

### 3.3. Inversion of Soil Moisture

In this study, an inversion scheme was developed that made use of the dual polarizations (HH and VV) available from the quad polarization Radarsat-2 data. After minimizing the effect of vegetation on the backscattering coefficient by the modified WCM, a look-up table (LUT) was developed to estimate soil moisture. To build the LUT, the parameters combinations were generated and used in the forward calculation of IEM. This method involved the creation of a table of backscattering coefficients associated with the surface soil moisture and roughness generated by performing multiple runs of the IEM within its validity range. To prevent too-wide parameter spaces and to reduce the size of the parameter spacing, the maximum and minimum values of soil moisture were fixed based on the prior knowledge from the field data collection. The implemented direct search algorithm attempts to minimize the merit function  $S$ , as shown in Equation (12), which represents differences between the measured and simulated backscattering coefficients.

$$S = \sqrt{\frac{1}{2}[(\sigma_{HH}^o - \sigma_{HHSAR}^o)^2 + (\sigma_{VV}^o - \sigma_{VVSAR}^o)^2]} \quad (12)$$

where  $\sigma_{HHSAR}^o$  and  $\sigma_{VVSAR}^o$  are the backscattering of the Radarsat-2 images at the HH polarization and at the VV polarization, respectively.  $\sigma_{HH}^o$  and  $\sigma_{VV}^o$  are the simulated backscattering at the HH polarization and at the VV polarization, respectively. The LUT is used to assess the best-fit value for  $\sigma_{HHSAR}^o$  and  $\sigma_{VVSAR}^o$  with a minimal  $S$ ; however, because of the measurement's uncertainty and the ill-posed inverse problem, the solution is usually not unique and is instead a range of estimated parameters. The mean value of the estimated parameters is taken as the estimated final result if the results are not unique. To verify the accuracy of this model inversion, a comparison is conducted between the measured and estimated soil moisture values using the correlation coefficient of determination ( $R^2$ ) and the RMSE.

## 4. Results and Discussion

### 4.1. Backscattering Simulations

The backscattering model was applied in its forward mode to simulate the total backscattering coefficients ( $\sigma_{total}^o$ ) using the surface parameters. Two-thirds of our data points from the field surveys (approximately 65 samples) were used to parameterize the backscattering model. The remaining one-third of the dataset (approximately 32 samples) was used to validate the model. To perform a comprehensive evaluation of modified backscattering model described in Section 3.2.2, the reproduced backscattering was achieved by applying the backscattering model described in Section 3.2.1 and modified backscattering model described in Section 3.2.2, respectively. Figure 2 shows scatterplots that represent the relationship between the SAR measured and predicted backscattering using the backscattering model described in Section 3.2.1 (Figure 2a is the scatterplot for HH polarization and Figure 2b is the scatterplot for VV polarization). The relationship between the measured and predicted backscattering (Figure 2) proved linear, but it had a moderate correlation ( $R^2 = 0.58$ ,  $p < 0.01$  for HH polarization;  $R^2 = 0.52$ ,  $p < 0.01$  for VV polarization). An interesting phenomenon is shown in Figure 2. The higher backscattering zone has larger deviations from the 1:1 lines than the lower backscattering

zone for both HH polarization and VV polarization. In other words, compared to the lower backscattering zone (backscattering less than  $-14$  dB for HH polarization; backscattering less than  $-17$  dB for VV polarization), the higher zone showed relatively higher correlations between the predicted and measured backscattering for both HH polarization and VV polarization. In previous studies [44,48], a negative relationship was found between backscattering and vegetation biomass. Therefore, the backscattering decreases with the increase of vegetation biomass. The backscattering decreased with increasing vegetation biomass at low values of the radar signal saturation because the decreasing contributions of soil roughness and moisture impacted the backscattering [49]. In this study, no samples were greater than the saturation level at the C-band ( $2.0 \text{ kg/m}^2$ ) [50]. Considering this claim, it can be assumed that errors in the backscattering model occurred mainly for the plots with relatively low vegetation densities. This phenomenon may be explained by the less-sensitive WCM for relatively sparse vegetation conditions. This view also supports the condition that volume scattering is the dominant mechanism responsible for the backscattering from vegetation when applying the WCM [26].

The backscattering was obtained assuming that the vegetation was homogeneous such that vegetation gap information was not accounted for in the backscattering model described in Section 3.2.1. Thus, the predicted backscattering was less accurate when gaps were present. In view of the sparse and patchy vegetation pattern, the applicability of the assumption was assessed by implementing the assumption only for the relative fraction of vegetation cover and by adding a backscattering component of the complementary soil fraction. The scatterplots demonstrate a strong linear correlation between the measured and predicted backscattering using the modified backscattering model (Figure 3a is the scatterplot for HH polarization and Figure 3b is the scatterplot for VV polarization). The predicted backscattering achieved by the modified backscattering model showed that the correlations between the measured and predicted backscattering was improved by including the effect of bare soil in the entire range of backscattering levels (for HH polarization,  $R^2$  increased from 0.58 to 0.79 and the RMSE decreased from 2.04 dB to 1.40 dB; for VV polarization,  $R^2$  increased from 0.52 to 0.77 and the RMSE decreased from 2.45 dB to 1.69 dB), especially for the higher backscattering zone (relatively sparse vegetation zone). This may indicate that the modified backscattering model has a higher sensitivity to relatively sparse vegetation conditions. The result demonstrated that the use of vegetation cover fractions could separate the scattering mechanisms of the fractions of vegetation cover and bare soil cover, and the accuracy of the backscattering modeling was significantly improved. The problem of sparse vegetation cover and the strong effect from bare soil patches could be minimized by implementing the modified model.

To understand the behavior of the model under different vegetation conditions, the results achieved terms of prediction accuracy (RMSE) and the goodness of fit ( $R^2$ ) are reported in Table 2. As observed in Table 2, backscattering modeled by the modified model demonstrated a significant improvement over the basic model under relatively sparse vegetation conditions, possibly suggesting that the modified model had a higher sensitivity to relatively sparse vegetation conditions. However, the accuracy did not vary significantly under the relatively density vegetation conditions. It may be because that the backscattering contribution of bare soil surfaces was a very small component in the total backscattering under the relatively density vegetation conditions.

**Figure 2.** Scatterplot illustrating the relationship between the measured backscattering from images and predicted backscattering values from the vegetation backscattering model described in Section 3.2.1 for (a) HH polarization and (b) VV polarization.

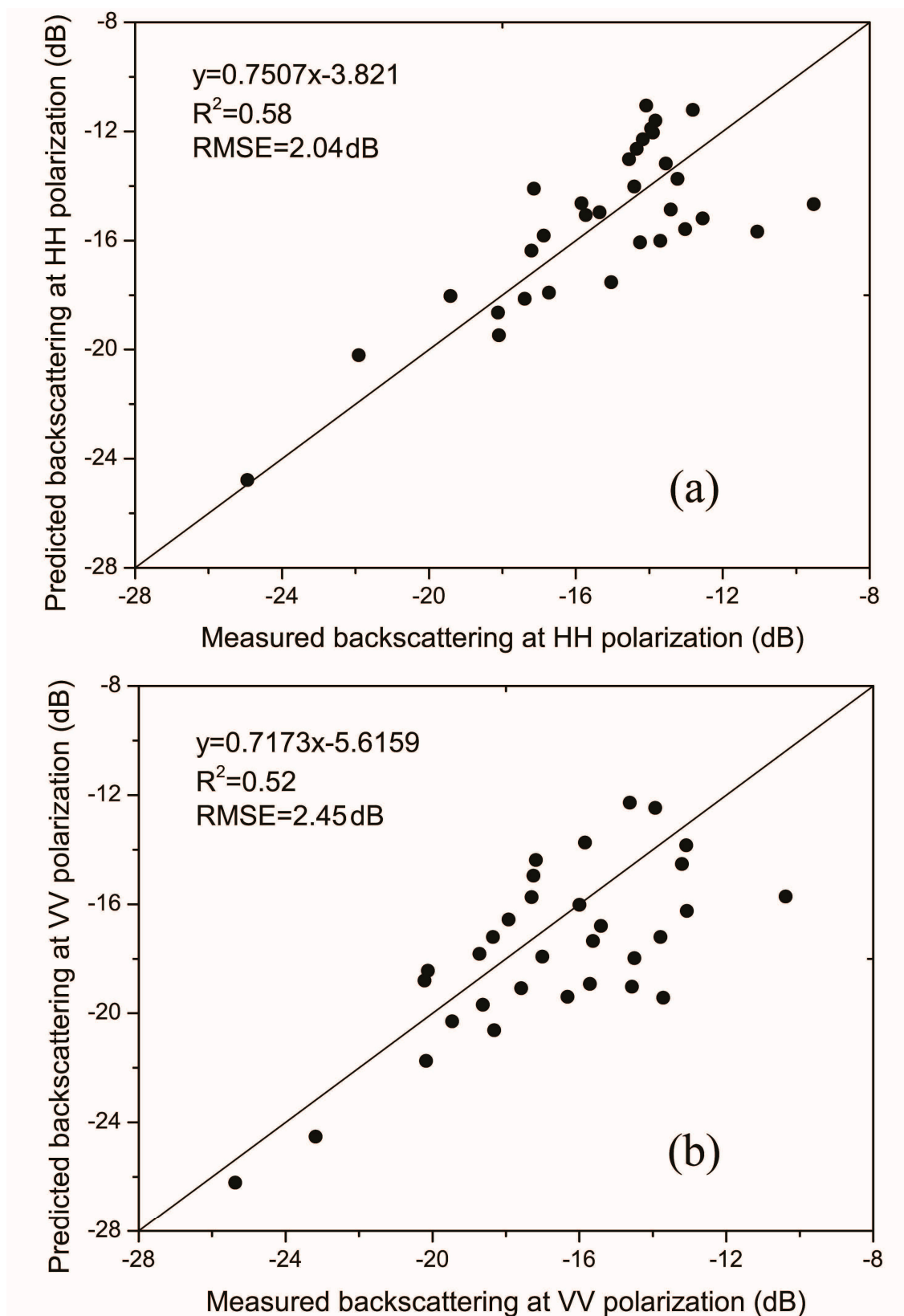


**Figure 3.** Scatterplot illustrating the relationship between the measured backscattering from the images and predicted backscattering values from the modified vegetation backscattering model described in Section 3.2.2 for (a) HH polarization and (b) VV polarization.

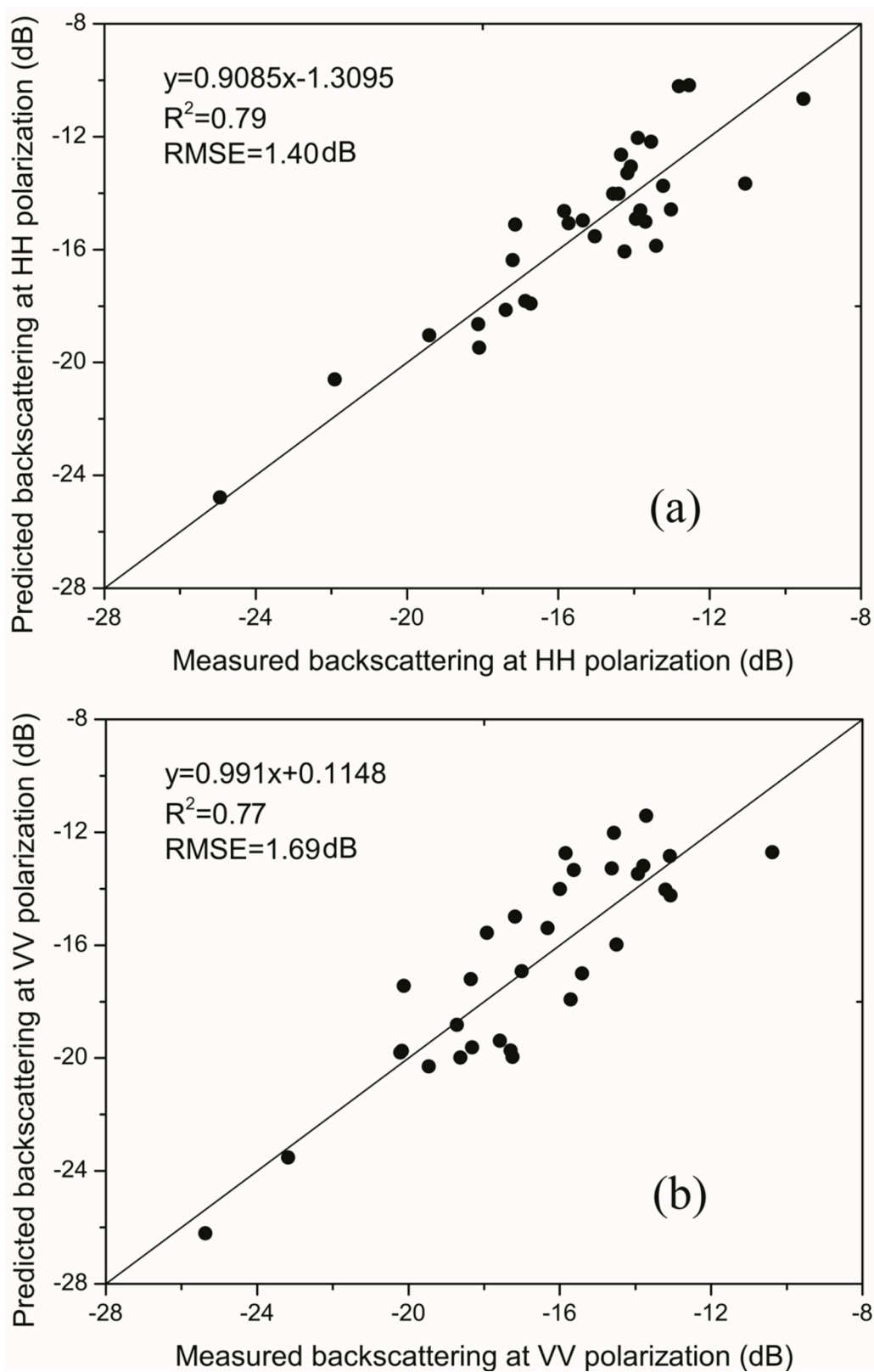


**Table 2.** Performance achieved on test samples using the basic model and modified model.

Vegetation condition	Model	HH Polarization		VV Polarization	
		$R^2$	RMSE	$R^2$	RMSE
<b>Density vegetation conditions</b>	Basic model	0.78	1.58	0.74	1.63
	Modified model	0.81	1.23	0.78	1.61
<b>Sparse vegetation conditions</b>	Basic model	0.25	2.65	0.15	2.93
	Modified model	0.73	1.77	0.74	1.79

To demonstrate the spatial performance of the proposed method in this study, the error of model simulation was defined as the absolute difference between the modeled and the Radarsat-2 SAR observed backscattering (dB):

$$error = \left| \sigma_{model}^o - \sigma_{SAR}^o \right| \quad (13)$$

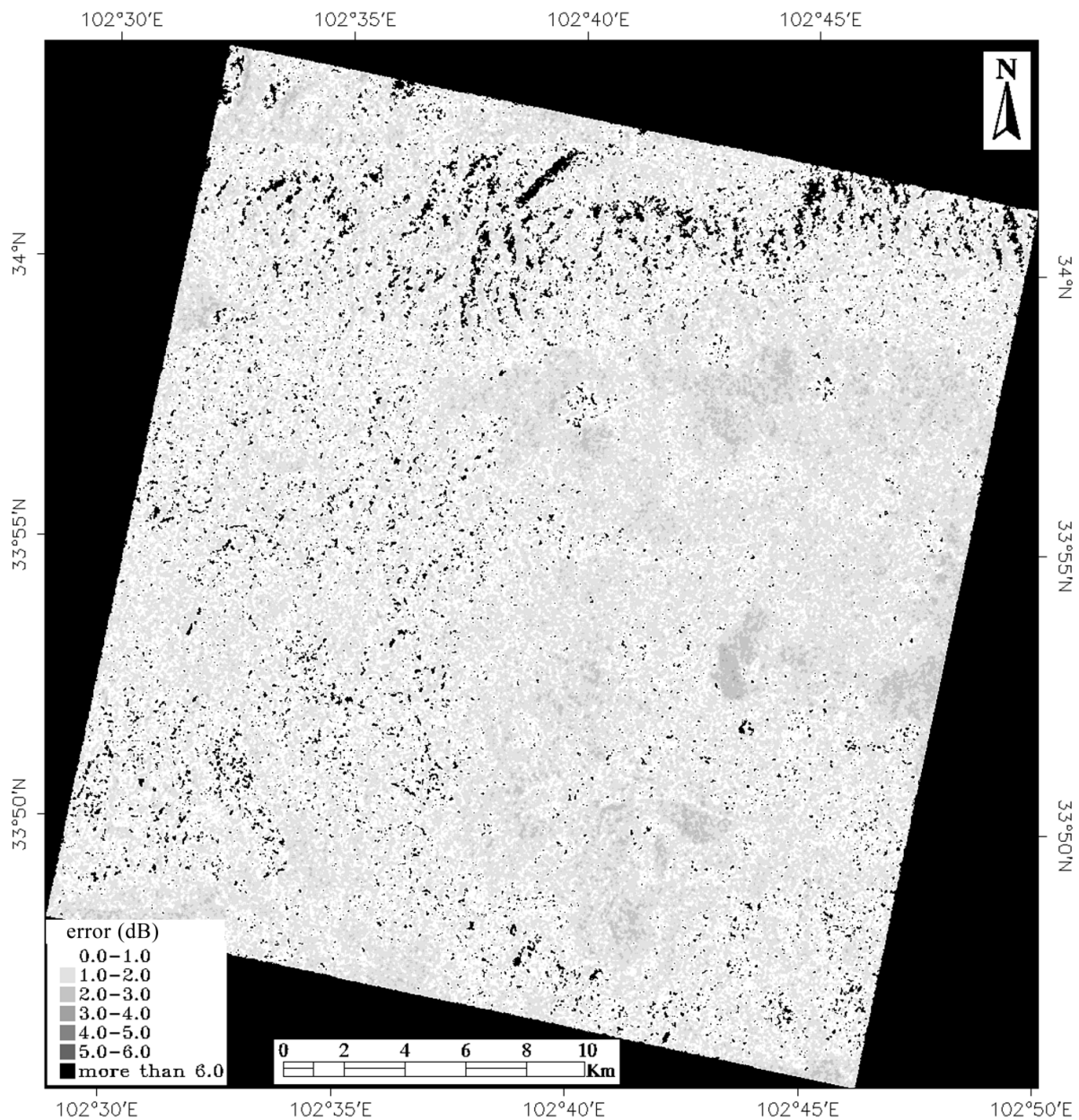
where  $\sigma_{model}^o$  and  $\sigma_{SAR}^o$  are the backscattering of the modeled and the observed backscattering, respectively.

Figure 4 shows the error map on 4 August 2013 for HH polarization. The areas with layovers and shadows were masked out in the process. Model errors for most of the study area were lower than 2 dB, indicating that the model simulation worked well in these areas. However, in the areas with high relief and steep slopes, model errors could be higher than 6 dB, suggesting that soil moisture estimation by model inversion was not reliable in these areas.

#### 4.2. Soil Moisture Estimation

The soil moisture estimation was performed by applying the LUT described in Section 3.3. Figure 5 shows the relationship between measured and predicted soil moisture when using the WCM to reduce the effect of vegetation. We observed that all the predicted soil moisture was overestimated when the soil moisture less than 19 vol.%. This phenomenon may be explained by the strong influence of vegetation. When the vegetation is characteristically sparse, the backscattering increment from vegetation exceeded the soil backscattering reduction due to vegetation attenuation [2]. The biomass of these plots is less than 0.3 kg/m<sup>2</sup>. Thus, the vegetation is sparse, it may cause that the attenuation on soil backscattering is lower than the backscattering increment from vegetation. Therefore, the soil moisture in these plots was overestimated.

The relationship between the measured and estimated volumetric soil moisture using the modified model is graphically represented in Figure 6. A linear relationship between the predicted and measured soil moisture (Figure 6) was observed, which suggests that the method described here could be effectively used to estimate soil moisture in an alpine prairie. However, as shown in Figure 6, the soil moisture values in wetter area had larger deviations from the 1:1 line than those in the relatively dryer area. In other words, there were larger retrieval errors in the wetter area than in the dryer area. This may be due to the high sensitivity of backscattering to changes in soil moisture with low soil water content; however, for wet soil, the backscattering is less sensitive [51]. This behavior may also be explained by the lower sensitivity of the IEM  $\sigma^o$  to soil moisture under wet conditions [52], and the IEM simulations show saturation behavior before the actual radar signals [53]. It may indicate that this method is problematic for estimating soil moisture under wet conditions.

**Figure 4.** The absolute error map of the model simulation.

The result reveals that volumetric soil moisture may be estimated with a maximum error of  $\pm 24.8\%$  (Figure 6). The errors in the soil moisture estimation were not merely from the simulation and inversion. They could also be partially caused by the data preprocessing. The main error sources that cause poor soil moisture estimates are as follows: (1) Because of measurement uncertainty and the ill-posed problem, the mean values were used as the inverse results when the solution was not unique. If a randomly solution was selected as the inverse result, the maximum error of the estimated soil moisture was  $\pm 64.6\%$ ; (2) Errors in the percentage of vegetation cover and LAI calculated from the optical imagery may have directly introduced errors into the soil moisture retrieval. The percentage of relative error was small for LAI; (3) In some areas of the image, the topography may cause errors in the inversion. Topographic distortions in the side-looking SAR image cannot be easily corrected in the mountainous area. As shown in Figure 4, model errors in the relatively flat area were lower than 2 dB. However, in the areas with high relief and steep slopes, model errors could be higher than 6 dB.

It suggesting that soil moisture estimation by model inversion was not reliable in these areas; (4) The acquisition times for the ascending and descending orbits of Radarsat-2 are different (morning and evening). The presence of dew drops in the morning may act to increase the dielectric constant of vegetation [54]. It may have directly introduced errors into the soil moisture retrieval. However, these error sources are not severe.

**Figure 5.** Scatterplot illustrating the relationship between the measured and predicted soil moisture when using the WCM to reduce the effect of vegetation.

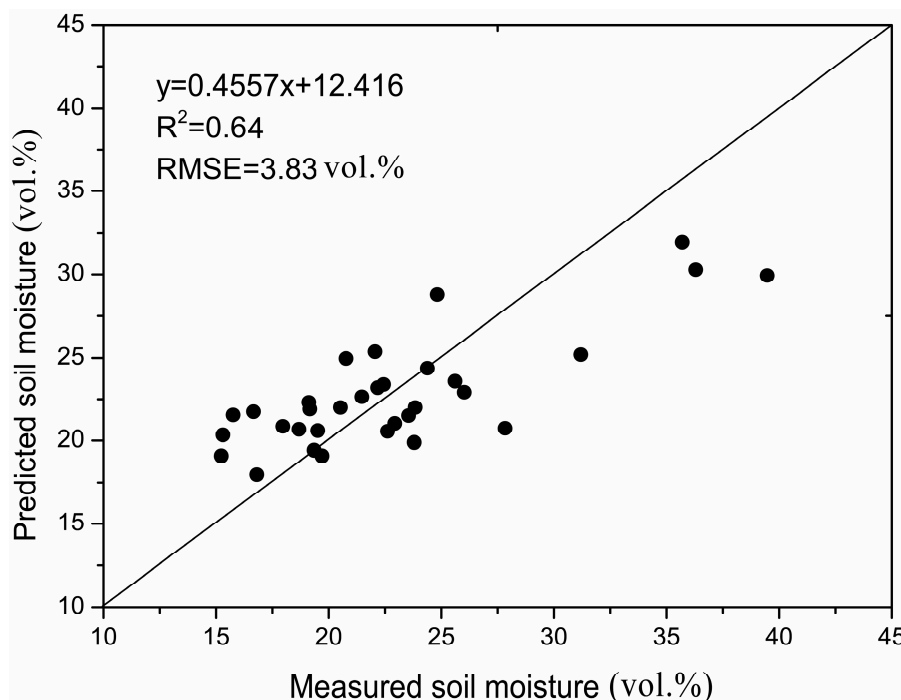
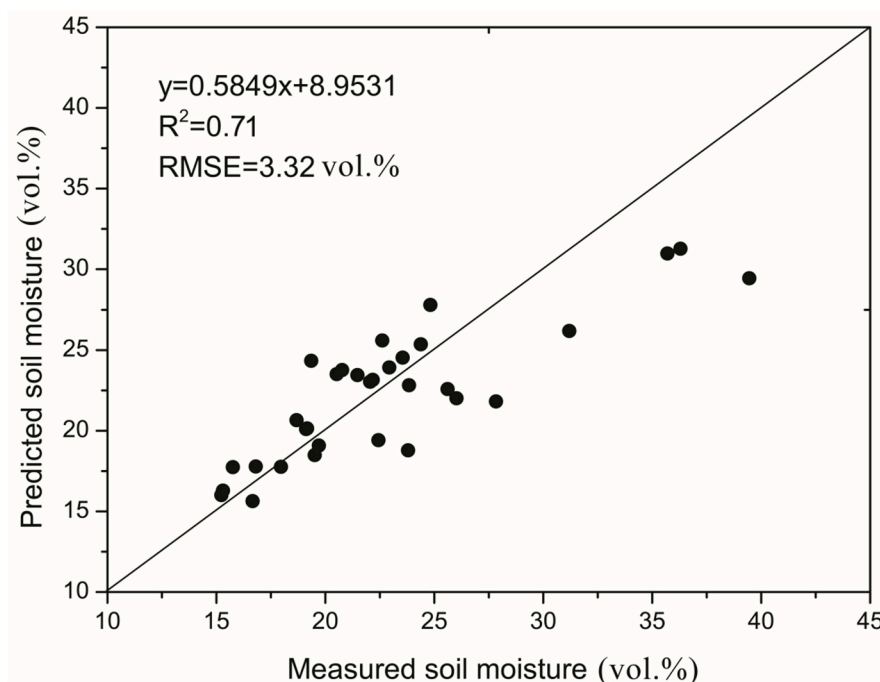


**Figure 6.** Scatterplot illustrating the relationship between the measured and predicted soil moisture when using the modified WCM to reduce the effect of vegetation.



## 5. Conclusions

This paper presents a microwave/optical synergistic method to estimate the soil moisture in a grassland area based on the IEM and modified WCM. To estimate the soil moisture using the IEM in a vegetated area, the vegetation contribution to the signal is removed with the use of the modified WCM. Then, the soil moisture over an alpine prairie was estimated from Radarsat-2 data.

Most of the previous studies on backscattering modeling of natural vegetation and agricultural crops assume that the vegetation is unified [44]. Therefore, it was difficult to use those models on a wide area where the vegetation ranged from fully to relatively sparse cover. In this method, the advantages of optical and microwave remote sensing methods were synthesized; the latter was used as the main method and the former as a supplementary method. The parameters retrieved by the optical model were the inputs to the microwave remote sensing model. The method uses vegetation coverage derived from optical data for calculating the contributions of the fractions of vegetation and bare soil at the pixel level to better represent the difference in the scattering mechanisms between vegetation and bare soil. The results show that the proposed approach can successfully predict backscattering from the alpine prairie. Furthermore, the capability of estimating soil moisture with this method is proven by quantitative comparisons between the measured and predicted values in the study area. These results demonstrate that the proposed method has a large potential for soil moisture retrieval of soils under vegetation because it can accurately estimate the soil moisture in areas that are either fully or sparsely covered by vegetation. Finally, the errors associated with the soil moisture estimation using this method were analyzed. It was found that the data preprocessing, model simulation and inversion could introduce errors into the soil moisture retrieval.

The estimated soil moisture information can be used to monitor the drought conditions of the prairie, which can guide the management of the grassland. In the near future, this model will be used to monitor the annual soil moisture changes in Ruoergai Prairie to study the grassland degradation and land desertification.

## Acknowledgments

This work was supported by the Fundamental Research Fund for the Central Universities (Contract No. ZYGX2012Z005), National Natural Science Foundation of China (Contract No. 41471293) and the National High-Tech Research and Development Program of China (Contract No. 2013AA12A302). The authors thank Xinwen Quan, Xing Li, Zhanmang Liao, Changming Yin, Zhi Wen, Junjie Hu, Wenying Zhou, Zhi Tang, Li Peng, and Shi Qiu for their assistance during the field measurements. We wish to thank four anonymous reviewers for their helpful comments and suggestions that substantially improved the manuscript. The DEM dataset was provided by the Geospatial Data Cloud, Computer Network Information Center, CAS (<http://www.gscloud.cn>).

## Author Contributions

Binbin He had the overall conception of the study. Minfeng Xing developed the methodology, performed the analysis and drafted the manuscript. Xiaojing Bai performed part of the data analysis.

## Conflicts of Interest

The authors declare no conflict of interest.

## References

1. Svoray, T.; Shoshany, M. Multi-scale analysis of intrinsic soil factors from SAR-based mapping of drying rates. *Remote Sens. Environ.* **2004**, *92*, 233–246.
2. Wang, C.; Qi, J.; Moran, S.; Marsett, R. Soil moisture estimation in a semiarid rangeland using ERS-2 and TM imagery. *Remote Sens. Environ.* **2004**, *90*, 178–189.
3. Oh, Y.; Sarabandi, K.; Ulaby, F.T. An empirical model and an inversion technique for radar scattering from bare soil surfaces. *IEEE Trans. Geosci. Remote Sens.* **1992**, *30*, 370–381.
4. Dubois, P.C.; van Zyl, J.; Engman, T. Measuring soil moisture with imaging radars. *IEEE Trans. Geosci. Remote Sens.* **1995**, *33*, 915–926.
5. Shi, J.; Wang, J.; Hsu, A.Y.; O'Neill, P.E.; Engman, E.T. Estimation of bare surface soil moisture and surface roughness parameter using L-band SAR image data. *IEEE Trans. Geosci. Remote Sens.* **1997**, *35*, 1254–1266.
6. Fung, A.K.; Li, Z.; Chen, K. Backscattering from a randomly rough dielectric surface. *IEEE Trans. Geosci. Remote Sens.* **1992**, *30*, 356–369.
7. Fung, A.K.; Chen, K. An update on the IEM surface backscattering model. *IEEE Geosci. Remote Sens. Lett.* **2004**, *1*, 75–77.
8. Chen, K.-S.; Wu, T.-D.; Tsang, L.; Li, Q.; Shi, J.; Fung, A.K. Emission of rough surfaces calculated by the integral equation method with comparison to three-dimensional moment method simulations. *IEEE Trans. Geosci. Remote Sens.* **2003**, *41*, 90–101.
9. Zribi, M.; Dechambre, M. A new empirical model to retrieve soil moisture and roughness from C-band radar data. *Remote Sens. Environ.* **2003**, *84*, 42–52.
10. Prakash, R.; Singh, D.; Pathak, N.P. A fusion approach to retrieve soil moisture with SAR and optical data. *IEEE J. Sel. Top. Appl. Earth Obs. Remote Sens.* **2012**, *5*, 196–206.
11. Bindlish, R.; Barros, A.P. Parameterization of vegetation backscatter in radar-based, soil moisture estimation. *Remote Sens. Environ.* **2001**, *76*, 130–137.
12. Sang, H.; Zhang, J.; Lin, H.; Zhai, L. Multi-polarization ASAR backscattering from herbaceous wetlands in Poyang Lake region, China. *Remote Sens.* **2014**, *6*, 4621–4646.
13. Lakhankar, T.; Ghedira, H.; Temimi, M.; Azar, A.E.; Khanbilvardi, R. Effect of land cover heterogeneity on soil moisture retrieval using active microwave remote sensing data. *Remote Sens.* **2009**, *1*, 80–91.
14. Notarnicola, C.; Angiulli, M.; Posa, F. Use of radar and optical remotely sensed data for soil moisture retrieval over vegetated areas. *IEEE Trans. Geosci. Remote Sens.* **2006**, *44*, 925–935.
15. Gherboudj, I.; Magagi, R.; Berg, A.A.; Toth, B. Soil moisture retrieval over agricultural fields from multi-polarized and multi-angular RADARSAT-2 SAR data. *Remote Sens. Environ.* **2011**, *115*, 33–43.
16. Du, J.; Shi, J.; Sun, R. The development of HJ SAR soil moisture retrieval algorithm. *Int. J. Remote Sens.* **2010**, *31*, 3691–3705.

17. Lievens, H.; Verhoest, N.E.C. On the retrieval of soil moisture in wheat fields from L-band SAR based on Water Cloud modeling, the IEM, and effective roughness parameters. *IEEE Geosci. Remote Sens. Lett.* **2011**, *8*, 740–744.
18. Roo, R.D.D.; Du, Y.; Ulaby, F.T.; Dobson, M.C. A semi-empirical backscattering model at L-band and C-band for a soybean canopy with soil moisture inversion. *IEEE Trans. Geosci. Remote Sens.* **2001**, *39*, 864–872.
19. Wang, C.; Qi, J. Biophysical estimation in tropical forests using JERS-1 SAR and VNIR imagery. II. Aboveground woody biomass. *Int. J. Remote Sens.* **2008**, *29*, 6827–6849.
20. Mattar, C.; Wigneron, J.-P.; Sobrino, J.A.; Novello, N.; Calvet, J.-C.; Albergel, C.; Richaume, P.; Mialon, A.; Guyon, D.; Jiménez-Muñoz, J.C. A combined optical–microwave method to retrieve soil moisture over vegetated areas. *IEEE Trans. Geosci. Remote Sens.* **2012**, *50*, 1404–1413.
21. Susan Moran, M.; Hymer, D.C.; Qi, J.; Sano, E.E. Soil moisture evaluation using multi-temporal synthetic aperture radar (SAR) in semiarid rangeland. *Agric. For. Meteorol.* **2000**, *105*, 69–80.
22. Santi, E.; Paloscia, S.; Pettinato, S.; Notarnicola, C.; Pasolli, L.; Pistocchi, A. Comparison between SAR soil moisture estimates and hydrological model simulations over the scrivina test site. *Remote Sens.* **2013**, *5*, 4961–4976.
23. Hosseini, M.; Saradjian, M. Soil moisture estimation based on integration of optical and SAR images. *Can. J. Remote Sens.* **2011**, *37*, 112–121.
24. Pasolli, L.; Notarnicola, C.; Bruzzone, L.; Bertoldi, G.; Della Chiesa, S.; Niedrist, G.; Tappeiner, U.; Zebisch, M. Polarimetric RADARSAT-2 imagery for soil moisture retrieval in alpine areas. *Can. J. Remote Sens.* **2011**, *37*, 535–547.
25. Paloscia, S.; Pettinato, S.; Santi, E.; Notarnicola, C.; Pasolli, L.; Reppucci, A. Soil moisture mapping using Sentinel-1 images: Algorithm and preliminary validation. *Remote Sens. Environ.* **2013**, *134*, 234–248.
26. Attema, E.; Ulaby, F.T. Vegetation modeled as a water cloud. *Radio Sci.* **1978**, *13*, 357–364.
27. Xiao, D.; Tian, B.; Tian, K.; Yang, Y. Landscape patterns and their changes in Sichuan Ruoergai Wetland National Nature Reserve. *Acta Ecol. Sin.* **2010**, *30*, 27–32.
28. Vermote, E.F.; Tanré, D.; Deuze, J.L.; Herman, M.; Morcette, J.J. Second simulation of the satellite signal in the solar spectrum, 6S: An overview. *IEEE Trans. Geosci. Remote Sens.* **1997**, *35*, 675–686.
29. Lee, J.-S.; Grunes, M.R.; de Grandi, G. Polarimetric SAR speckle filtering and its implication for classification. *IEEE Trans. Geosci. Remote Sens.* **1999**, *37*, 2363–2373.
30. Loew, A.; Mauser, W. Generation of geometrically and radiometrically terrain corrected SAR image products. *Remote Sens. Environ.* **2007**, *106*, 337–349.
31. Van Zyl, J.J.; Chapman, B.D.; Dubois, P.; Shi, J. The effect of topography on SAR calibration. *IEEE Trans. Geosci. Remote Sens.* **1993**, *31*, 1036–1043.
32. Pairman, D.; Belliss, S.E.; McNeill, S.J. Terrain influences on SAR backscatter around Mt. Taranaki, New Zealand. *IEEE Trans. Geosci. Remote Sens.* **1997**, *35*, 924–932.
33. Zribi, M.; le Hégarat-Masclé, S.; Ottlé, C.; Kammoun, B.; Guerin, C. Surface soil moisture estimation from the synergistic use of the (multi-incidence and multi-resolution) active microwave ERS Wind Scatterometer and SAR data. *Remote Sens. Environ.* **2003**, *86*, 30–41.

34. Merzouki, A.; McNairn, H.; Pacheco, A. Mapping soil moisture using RADARSAT-2 data and local autocorrelation statistics. *IEEE J. Sel. Top. Appl. Earth Obs. Remote Sens.* **2011**, *4*, 128–137.
35. Jacome, A.; Bernier, M.; Chokmani, K.; Gauthier, Y.; Poulin, J.; de Sève, D. Monitoring volumetric surface soil moisture content at the la grande basin boreal wetland by radar multi polarization data. *Remote Sens.* **2013**, *5*, 4919–4941.
36. Topp, G.; Davis, J.; Annan, A.P. Electromagnetic determination of soil water content: Measurements in coaxial transmission lines. *Water Resour. Res.* **1980**, *16*, 574–582.
37. Biftu, G.F.; Gan, T.Y. Retrieving near-surface soil moisture from Radarsat SAR data. *Water Resour. Res.* **1999**, *35*, 1569–1579.
38. Magagi, R.; Bernier, M.; Ung, C. Quantitative analysis of RADARSAT SAR data over a sparse forest canopy. *IEEE Trans. Geosci. Remote Sens.* **2002**, *40*, 1301–1313.
39. Moran, M.S.; Vidal, A.; Troufleau, D.; Inoue, Y.; Mitchell, T.A. Ku-and C-band SAR for discriminating agricultural crop and soil conditions. *IEEE Trans. Geosci. Remote Sens.* **1998**, *36*, 265–272.
40. Prévot, L.; Champion, I.; Guyot, G. Estimating surface soil moisture and leaf area index of a wheat canopy using a dual-frequency (C and X bands) scatterometer. *Remote Sens. Environ.* **1993**, *46*, 331–339.
41. Jacquemoud, S.; Verhoef, W.; Baret, F.; Bacour, C.; Zarco-Tejada, P.J.; Asner, G.P.; François, C.; Ustin, S.L. PROSPECT+ SAIL models: A review of use for vegetation characterization. *Remote Sens. Environ.* **2009**, doi:10.1016/j.rse.2008.01.026.
42. Inoue, Y.; Kurosu, T.; Maeno, H.; Uratsuka, S.; Kozu, T.; Dabrowska-Zielinska, K.; Qi, J. Season-long daily measurements of multifrequency (Ka, Ku, X, C, and L) and full-polarization backscatter signatures over paddy rice field and their relationship with biological variables. *Remote Sens. Environ.* **2002**, *81*, 194–204.
43. Ulaby, F.T.; Sarabandi, K.; McDonald, K.; Whitt, M.; Dobson, M.C. Michigan microwave canopy scattering model. *Int. J. Remote Sens.* **1990**, *11*, 1223–1253.
44. Svoray, T.; Shoshany, M. SAR-based estimation of areal aboveground biomass (AAB) of herbaceous vegetation in the semi-arid zone: A modification of the water-cloud model. *Int. J. Remote Sens.* **2002**, *23*, 4089–4100.
45. Svoray, T.; Shoshany, M. Herbaceous biomass retrieval in habitats of complex composition: A model merging SAR images with unmixed Landsat TM data. *IEEE Trans. Geosci. Remote Sens.* **2003**, *41*, 1592–1601.
46. Xing, M.; He, B.; Li, X. Integration method to estimate above-ground biomass in arid prairie regions using active and passive remote sensing data. *J. Appl. Remote Sens.* **2014**, doi:10.1117/1.JRS.8.083677.
47. Gutman, G.; Ignatov, A. The derivation of the green vegetation fraction from NOAA/AVHRR data for use in numerical weather prediction models. *Int. J. Remote Sens.* **1998**, *19*, 1533–1543.
48. Taconet, O.; Benallegue, M.; Vidal-Madjar, D.; Prévot, L.; Dechambre, M.; Normand, M. Estimation of soil and crop parameters for wheat from airborne radar backscattering data in C and X bands. *Remote Sens. Environ.* **1994**, *50*, 287–294.
49. Svoray, T.; Shoshany, M.; Curran, P.; Foody, G.M.; Perevolotsky, A. Relationship between green leaf biomass volumetric density and ERS-2 SAR backscatter of four vegetation formations in the semi-arid zone of Israel. *Int. J. Remote Sens.* **2001**, *22*, 1601–1607.

50. Imhoff, M.L. Radar backscatter and biomass saturation: Ramifications for global biomass inventory. *IEEE Trans. Geosci. Remote Sens.* **1995**, *33*, 511–518.
51. Bindlish, R.; Barros, A.P. Multifrequency soil moisture inversion from SAR measurements with the use of IEM. *Remote Sens. Environ.* **2000**, *71*, 67–88.
52. Joseph, A.; van der Velde, R.; O’Neill, P.; Lang, R.; Gish, T. Effects of corn on C-and L-band radar backscatter: A correction method for soil moisture retrieval. *Remote Sens. Environ.* **2010**, *114*, 2417–2430.
53. Zribi, M.; Baghdadi, N.; Holah, N.; Fafin, O. New methodology for soil surface moisture estimation and its application to ENVISAT-ASAR multi-incidence data inversion. *Remote Sens. Environ.* **2005**, *96*, 485–496.
54. Kasischke, E.S.; Bourgeau-Chavez, L.L. Monitoring south Florida wetlands using ERS-1 SAR imagery. *Photogramm. Eng. Remote Sens.* **1997**, *63*, 281–291.

© 2014 by the authors; licensee MDPI, Basel, Switzerland. This article is an open access article distributed under the terms and conditions of the Creative Commons Attribution license (<http://creativecommons.org/licenses/by/4.0/>).